PCCP

ROYAL SOCIETY OF CHEMISTRY

PAPER

View Article Online
View Journal | View Issue

Cite this: *Phys. Chem. Chem. Phys.*, 2024, **26**, 2093

High-throughput computational materials screening of transition metal peroxides†

Yin-Hui Peng, Chang-Chun He, Yu-Jun Zhao and Xiao-Bao Yang *

Received 18th August 2023,
Accepted 23rd November 2023

DOI: 10.1039/d3cp03968d

rsc.li/pccp

Semiconductor materials of abnormal stoichiometric ratio often exhibit unique properties, yet it is still a challenge to determine the structures of such materials in an efficient way. Herein, we propose a method for structurally biased screening according to the coordination numbers and the numbers of Wyckoff positions, balancing the atom local environment and the global symmetry of structures. Based on first-principles calculations, we have predicted two metastable peroxides $P2_1/c$-ScO_2 and $Pmmn$-TiO_3 with more than six coordination points. For these two structures, the most stable intrinsic defect is the oxygen vacancy (V_O) at the peroxide anion (O_2^{2-}), which induces the absence of antibonding orbital π_g^* formed by O_2^{2-} near the valence band maximum. With the introduction of V_O, the decrease of coordination numbers leads to charge recombination, and results in the appearance of an ordered phase $TiO_{2.5}$ with stronger Ti–O orbital hybridization. The proposed method presents a promising and feasible approach for the screening of novel compounds.

1 Introduction

The pursuit of metal oxide semiconductor materials with outstanding performance has consistently attracted significant attention.[1–3] For instance, In_2O_3, Ga_2O_3, ZnO and TiO_2 have found widespread applications in various fields including flat-panel displays, solar cells, flexible and catalytic processes.[4,5] The stoichiometric ratios and crystal structures of stable oxide semiconductors can be modulated by ambient factors such as temperature, pressure, and oxygen in the environment. Experimentally, the discovery and application of semiconductor materials with varying stoichiometric ratios has predominantly relied on trial-and-error methods, which have proved to be incomplete and time-consuming for the majority of samples.[6] On the contrary, theoretical high-throughput methods enable the rapid and comprehensive prediction of ordered stable structures. Materials with a high concentration of defects like $Sc_{1-x}S$,[7] TiN_{1-x},[8] and $NaCl_{1-x}$,[9] can be derived from the rock salt structure prototype through ordered vacancy arrangements. Similarly, other structures also exhibit spontaneous high concentration vacancies, such as Ba_4As_{3-x}, $Ag_{3-x}Al_{22}O_{34}$, and $Ba_{1-x}NbO_3$.[10] After determining the atomic distributions, theoretical calculations have further demonstrated the physical and chemical properties of the new materials, including their electronic, mechanical, and magnetic properties.[11–14]

In order to predict novel structures, researchers commonly employ structure search software such as RG^2,[15] USPEX,[16] and CALYPSO.[17] Novel structures such as TiO_3,[18,19] YO_3,[20] VO_4,[21] CaO_3,[22] LaS_2,[23] have been predicted to be stable at high pressure, but they have not yet been included in crystal structure databases, such as the Material Project Database,[24] the AFLOWLIB Database,[25] and the Open Quantum Materials Database.[26] In the global structure optimization, the computing of a sufficient number of structures is required to establish an accurate potential energy surface, and the diversity of structures will significantly increase the difficulty of predicting multi-component systems. Other global optimization algorithms, such as following imaginary phonons,[27] simulated annealing,[28] basin and minima hopping,[29,30] metadynamics,[31] and evolutionary algorithms,[32] have also attracted much attention.[33] The continuous accumulation of theoretical calculations and experiments has significantly expanded the crystal database, providing abundant crystal structures for high-throughput material screening.[34] High-throughput calculations involving the screening of potential candidate structures from a vast alloy space also require substantial computational resources.[35] Although machine learning models trained on large datasets can help alleviate the computational burden, they often suffer from limitations in migration and expansion capabilities.[36] Compared with these methods, the biased screening is practical and efficient to generate the potential candidates with high stabilities or expected properties.[37]

In this work, we have utilized the structures from the AFLOWLIB database to conduct high-throughput structure screening.[25] By applying the biased screening based on coordination numbers

School of Physics and Optoelectronics, South China University of Technology, Guangzhou 510640, China. E-mail: scxbyang@scut.edu.cn

† Electronic supplementary information (ESI) available. See DOI: https://doi.org/10.1039/d3cp03968d

(N_c) and numbers of Wyckoff positions (N_w), we have efficiently predicted structures such as ScO_2 and TiO_3 with dynamical stability. Additionally, the discovered structures provide insights into the coordination rules governing peroxides. The stability of these structures is closely associated with O_2^{2-} induced by high N_c, and the electronic structure is analyzed to provide a reasonable explanation of the structural stability.

2 Computational methods

In all simulations, we have employed the Vienna Ab initio simulation package (VASP) based on density functional theory.[38,39] The Perdew–Burke–Ernzerhof (PBE) generalized gradient approximation was chosen to describe the exchange–correlation interaction.[40,41] A cutoff energy of 520 eV and a spacing of 0.2 $Å^{-1}$ between the k-points in the Brillouin zone were used to ensure energy convergence to 1 meV per atom. The residual atomic forces were constrained to a criteria of 0.02 eV $Å^{-1}$. Phonopy code with the finite displacement approach was employed to confirm the dynamical stabilities of the predicted structures.[42,43] For the evaluation of thermal stability, we used Ab initio molecular dynamics (AIMD) simulations at 500 K. Those simulations were performed in the *NVT* ensemble for a duration of 9 ps with a time step of 1.0 fs, and the kinetic temperature was controlled by the Nosé–Hoover method.[44]

The formation energy ($\Delta H_D^{(\alpha,q)}$) of defect α and the average formation energy (ΔE_{V_O}) with different numbers of oxygen vacancies can be calculated as follows:[45]

$$\Delta H_D^{(\alpha,q)} = E(\alpha,q) - E(0) + \sum_\alpha n_\alpha\left(\Delta\mu_\alpha + \mu_\alpha^{solid}\right) + q(E_{VBM} + E_f) \quad (1)$$

$$\Delta E_{V_O} = \Delta H_D^{(V_O,0)} \Big/ |n_{V_O}| \quad (2)$$

where $E(\alpha,q)$ and $E(0)$ are the total energy of the supercell with and without defect α, respectively. n_α is the number of defect α. A positive or negative value of n_α indicates the atoms are removed or added, respectively. The q is the defect charge state. The E_{VBM} is the energy at the VBM of perfect structure, and E_f is the Fermi energy relative to the E_{VBM}. μ_α is the total energy of the most stable phase corresponding to defect α. Here is the oxygen molecule, bulk *P*6/*mmm*-Ti and *Cmcm*-Sc.

3 Results and discussion

The AFLOWLIB database provides a rich source of candidate structures for transition metal peroxides,[25] as shown in Fig. 1(a). We extracted all non-equivalent binary metal and nonmetallic structures from the AFLOWLIB database, resulting in a total of 10 947 structures. Among the transition metal oxides, the six coordination motif is energetically preferable, with the metal atoms adopting an octahedral configuration surrounded by oxygen atoms. Furthermore, peroxides often follow supercoordination rules, as observed in compounds like Li_2O_2,[46] and Na_2O_2.[47] Based on the characteristics of stable structures, the metal atoms with six or more coordination in the local environment were selected, totalling 1093. Our previous studies have shown that structures with smaller N_w tend to be more stable in binary alloys.[48] According to the global symmetry of structure, we further refined the candidate structures with N_w less than four. The N_s varies with N_c and N_w as shown in Fig. 1(b). We find that N_c and N_w serve as useful indicators that can substantially reduce the computational cost. We utilize the 554 candidate structures indicated by the arrows in Fig. 1(b) for our following calculations.

3.1 Dynamically stable crystal structures of TiO_3 and ScO_2

Based on the high-throughput first principles calculations, we have obtained formation enthalpies of possible TiO_x and ScO_x candidates as shown in Fig. S1 (ESI†). All of the structures residing in the convex hull are considered stable, while those positioned above the convex hull are categorized as metastable. Specifically, the $P2_1/c$-ScO_2 and *Pmmn*-TiO_3 structures, as displayed in Fig. 2(a) and (d), are identified as metastable. Compared with the $P2_1/c$ and $Pm\bar{3}n$ TiO_3 predicted by previous

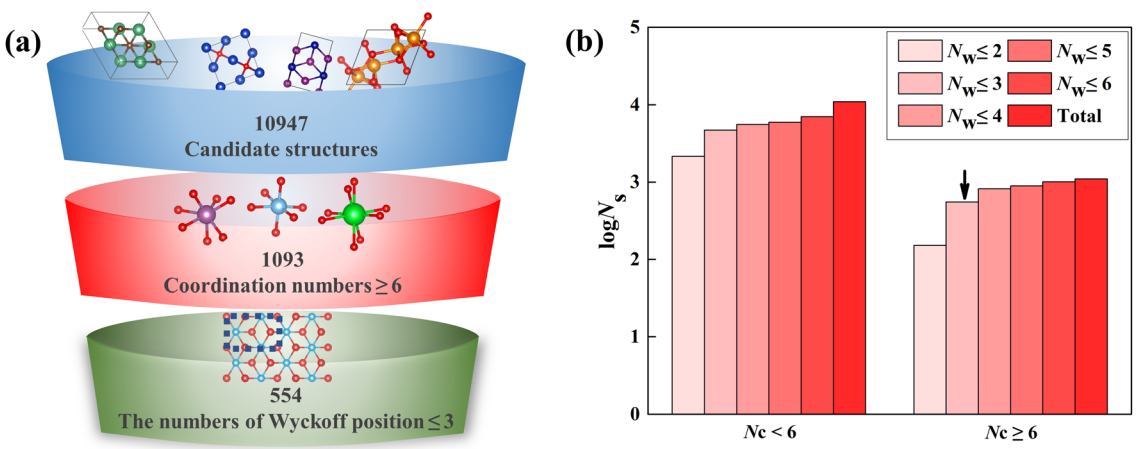

Fig. 1 (a) Framework for high-throughput material screening of transition metal peroxides based on the Wyckoff position and coordination numbers. (b) The number of structures (N_s) in a certain number of Wyckoff positions (N_w) and with certain coordination number (N_c).

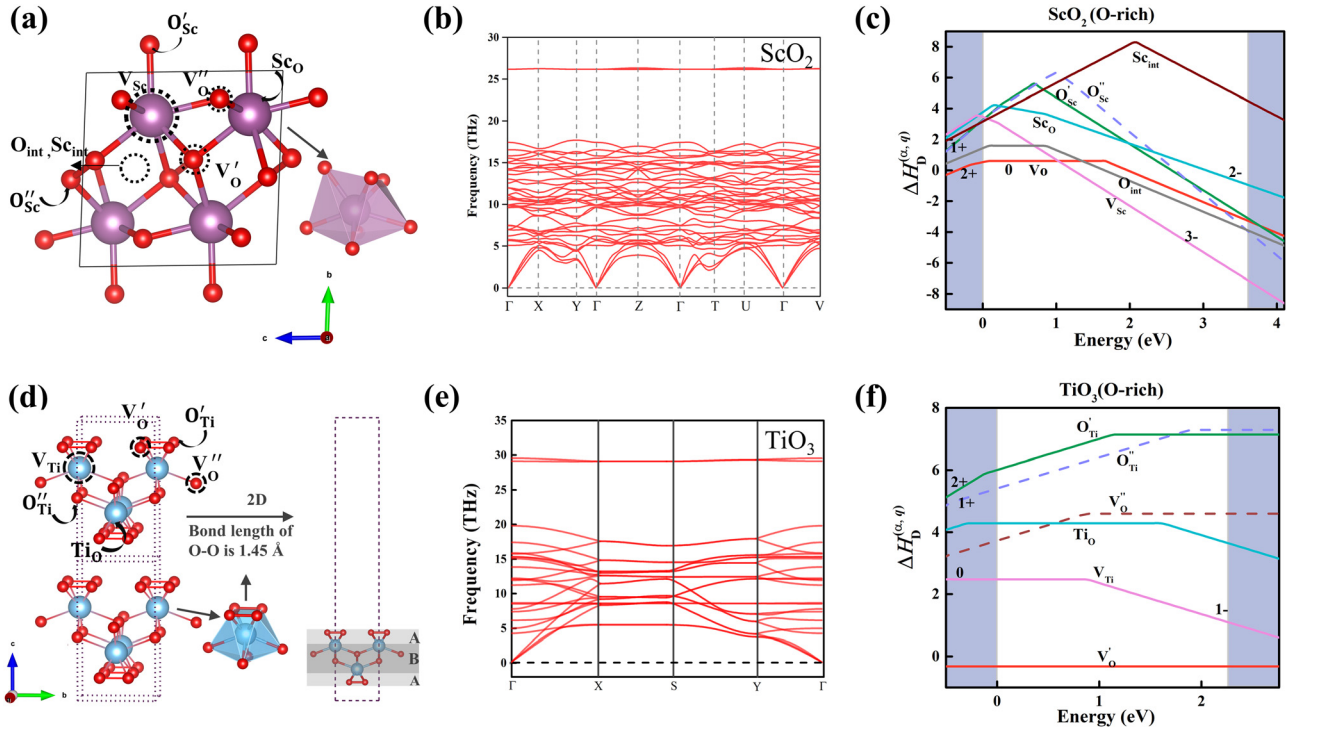

Fig. 2 (a) and (d) Structures and defect types of the bulk ScO_2 and layered TiO_3. (b) and (e) Phonon-dispersion spectrum for ScO_2 and TiO_3. (c) and (f) The formation energies of the intrinsic point defect as a function of the Fermi level for ScO_2 with a 3 × 2 × 2 supercell and single layered TiO_3 with a 4 × 3 × 1 supercell.

work, the total energy of the *Pmmn*-TiO_3 respectively decreases by 1.41 and 2.75 eV per f.u.[18,19] The detailed crystal information for both the $P2_1/c$-ScO_2 and *Pmmn*-TiO_3 structures can be found in the ESI,† Table S1.

To evaluate the dynamical stability, we calculated the phonon spectrum for the bulk $P2_1/c$-ScO_2 and single layered *Pmmn*-TiO_3 using a primitive cell as shown in Fig. 2(b) and (e). We isolated a single layer of the *Pmmn*-TiO_3 from the bulk structure and added a vacuum of 18 Å perpendicular to the plane, to prevent the interactions between the periodic replicas in the out-of-plane direction, as shown on the right of image Fig. 2(d). The absence of any negative phonon frequencies confirms the dynamical stability of the structures in our predictions. Moreover, we performed AIMD at 500 K using a 4 × 3 × 3 supercell of ScO_2 and a 6 × 4 × 1 supercell of TiO_3 to assess the thermodynamic stability, as shown in Fig. S2(a) and (b) (ESI†). The fluctuations of the total energy and temperature are negligible, indicating high thermodynamic stability. For the single layered *Pmmn*-TiO_3, the cleavage energy was found to be 0.32 J m^{-2}, as shown in Fig. S2(c) (ESI†). The value is smaller than the cleavage energies of many proposed two-dimensional (2D) materials, such as GeP_3 (1.14 J m^{-2}),[49] InP_3 (1.32 J m^{-2}),[50] Ca_2N (1.09 J m^{-2}),[51] and SnP_3 (0.71 J m^{-2}).[50] The proximity of the cleavage energy for TiO_3 to that of our calculated graphene (0.3 J m^{-2}) suggests that the single layered TiO_3 may be relatively easy to cleave from the bulk phase using either mechanical or liquid exfoliation processes.

In the ScO_2 structure, the Sc atom is surrounded by seven O atoms, containing one O_2^{2-} and six O^{2-}. As shown in Fig. 2(a), the O–O bond length is 1.47 Å. The structure has a total of three Wyckoff positions, including two non-equivalent O atoms and one Sc atom. For the TiO_3, the Ti atom is surrounded by eight O atoms, containing two pairs of O_2^{2-} and four O^{2-}. The structure obeys the rule of square antiprisms in metal octahedra,[52] and has three Wyckoff positions. As shown in Fig. 2(d), the lattice information of the TiO_3 follows an ABA sequence, and the O_2^{2-} bond length in the surface layer is 1.45 Å. Regardless of ScO_2 or TiO_3, the screening condition of N_c ensures the presence of an informal oxidation state, leading to the formation of O_2^{2-}. The Bader charge shown in the ESI,† Table S2, also shows that the charge obtained by the O_2^{2-} is the same as O^{2-}. Thus, we can conclude that both the O^{2-} and O_2^{2-} have captured two electrons. In most cases, when the sum of composition weighed oxidation state is zero, these compounds are typically insulators or semiconductors. In the case of ScO_2, it can be regarded as having one +3 valence for Sc^{3+}, one +2 valence for O^{2-} and a half of O_2^{2-} with +2 valence. For the TiO_3, it can be regarded as having one +4 valence Ti, one +2 valence O^{2-}, and one O_2^{2-} with +2 valence. Therefore, the appearance of band gaps for transition metal peroxides are primarily regulated by the ratio of O_2^{2-} and O^{2-}.

During the synthesis of materials, defects are inevitable, especially in transition metal peroxides. Therefore, for the ScO_2, we consider several intrinsic defects, including oxygen vacancies (V'_O, V''_O, at different positions), scandium vacancy (V_{Sc}), interstitial oxygen and scandium (O_{int}, Sc_{int}), and antisite defects (Sc_O, O_{Sc}), as shown in Fig. 2(a). We used a 3 × 2 × 2 supercell to calculate the formation energies corresponding to

these defects, as shown in Fig. 2(c). For both types of oxygen vacancies, V'_O and V''_O, will result in the same configuration after structural relaxation, and the $\Delta H_D^{(V_O,0)}$ are 0.64 eV in neutral V_O. With the Fermi level over the 1 eV, the V_{Sc}^{3-} is energetically favorable. Since the TiO_3 is a 2D material, we calculated the intrinsic defects in a 4 × 3 × 1 supercell, only including V'_O, V''_O, titanium vacancy (V_{Ti}), and antisite defects (Ti_O, O'_{Ti}, O''_{Ti}), as shown in Fig. 2(d). It has been found that introducing the V'_O in layer A is energetically favorable, and the $\Delta H_D^{(\alpha)}$ is low up −0.39 eV, as shown in Fig. 2(f).

Based on the crystal orbital Hamilton populations (COHP) as shown in Fig. S2(d) (ESI†), we confirm that the O_2^{2-} exhibit antibonding orbitals below the valence band maximum (VBM) in both ScO_2 and TiO_3, thus reducing the structural stability. This finding provides a comprehensive explanation for introducing one oxygen vacancy in O_2^{2-} as the most stable intrinsic defect in transition metal peroxides. The presence of antibonding orbitals caused by the O_2^{2-} is also common in metal peroxides such as Li_2O_2.[46]

Negative $\Delta H_D^{(\alpha)}$ indicates that a structure with a high concentration of oxygen vacancies might be stable in the layered TiO_3. To determine the defect concentration of oxygen vacancies in the 2D *Pmmn*-TiO_3, we enumerate all configurations of V_O using the Structures of Alloy Generation and Recognition (SAGAR) method.[37] Considering the $\Delta H_D^{(\alpha)}$ for TiO_3, we find that the V_O in layer A has a much lower $\Delta H_D^{(\alpha)}$ compared with other intrinsic defects. Thus, we focus on structures containing V_O in layer A using a 2 × 2 × 1 supercell. In Fig. 3(a), the average formation energies ΔE_{V_O}, varying with oxygen vacancy concentration are given. The most stable structure is $TiO_{2.5}$ corresponding to the ΔE_{V_O} of −0.45 eV. The red and blue triangles in the figure correspond to the two types of oxygen vacancy. One is where the single peroxide anion O_2^{2-} loses at most one O atom to form a bridging oxygen anion (O_b^{2-}), and the other is that the structure loses at least one complete O_2^{2-}. Fig. 4(b) shows both types of structure in a 2 × 2 × 1 supercell, and the ΔE_{V_O} of the former is 2.73 eV lower than that of the latter. When the oxygen defect configurations have lost at least one complete O_2^{2-} in TiO_3, the structural stability is so low.

In order to fully investigate the distribution of oxygen vacancies, we use the $\sqrt{5} \times \sqrt{5} \times 1$ and 3 × 3 × 1 supercell to eliminate the influence of the cell size on the structural stability. Taking into account that the O_b^{2-} is energetically preferable, only the V_O are introduced at the red ball's, as shown in Fig. 3(c). All ΔE_{V_O} are less than zero as shown in Fig. S3(a) (ESI†), which strongly supports the validity of searching for the distributions of O_b^{2-}. The most stable structure is still the $TiO_{2.5}$ in a 2 × 2 × 1 supercell. To ensure that the defective phases fail to separate, we have used perfect TiO_3 and TiO_2 with layer A filled O_b^{2-} as the reference phases, and given the convex hulls of formation enthalpy (ΔE_f) as shown in Fig. 3(c). The calculated formula is defined as follows:

$$\Delta E_f(TiO_{3-x}) = E(TiO_{3-x}) - (1-x)E(TiO_3) - xE(TiO_2) \quad (3)$$

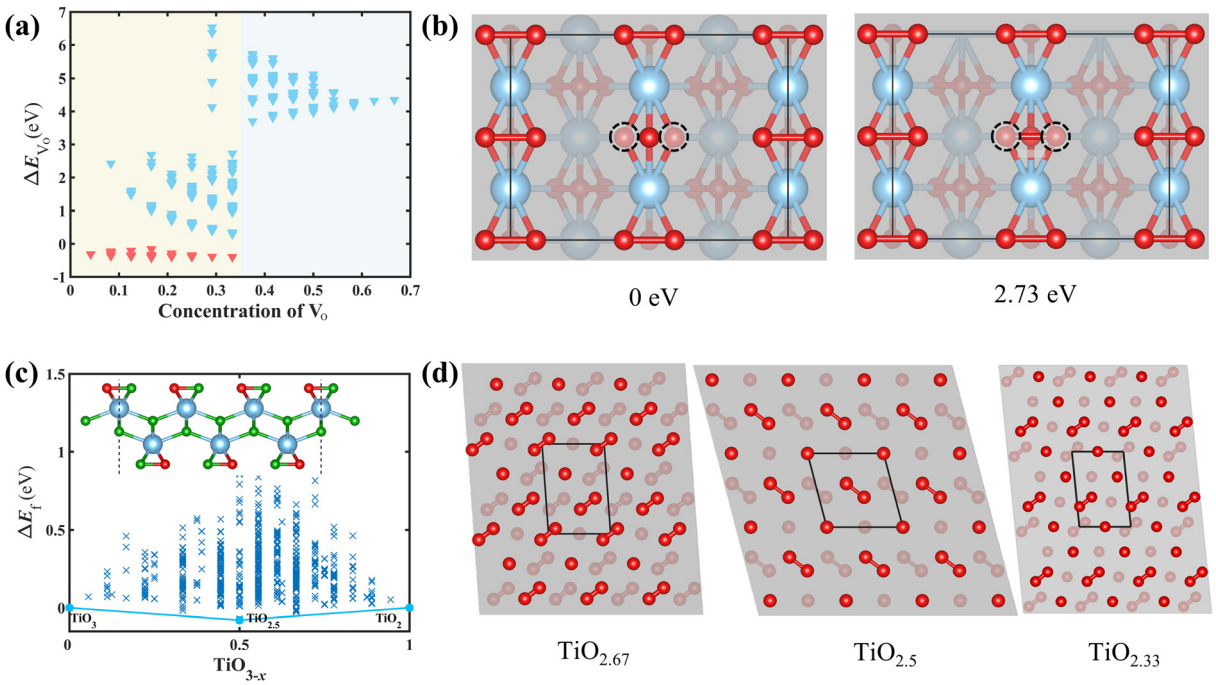

Fig. 3 (a) The average formation energy ΔE_{V_O} varies with oxygen vacancy concentration for a 2 × 2 × 1 supercell in TiO_3. The red triangles represent the configuration in which the O_2^{2-} loses at most one O atom, while the blue triangle indicates that the structure loses at least one complete O_2^{2-}. (b) Structures introducing single and double oxygen vacancies in the layer A of the 2 × 2 × 1 supercell TiO_3. (c) The convex hulls of the enthalpy of formation ΔE_f with the perfect TiO_3 and TiO_2 as reference phases. The red balls in the structure indicate where oxygen vacancies are introduced. (d) The structure diagram of $TiO_{2.67}$, $TiO_{2.5}$ and $TiO_{2.33}$. The dark red balls represent the upper layer A of the structure, and the light red balls represent the lower layer A of the structure.

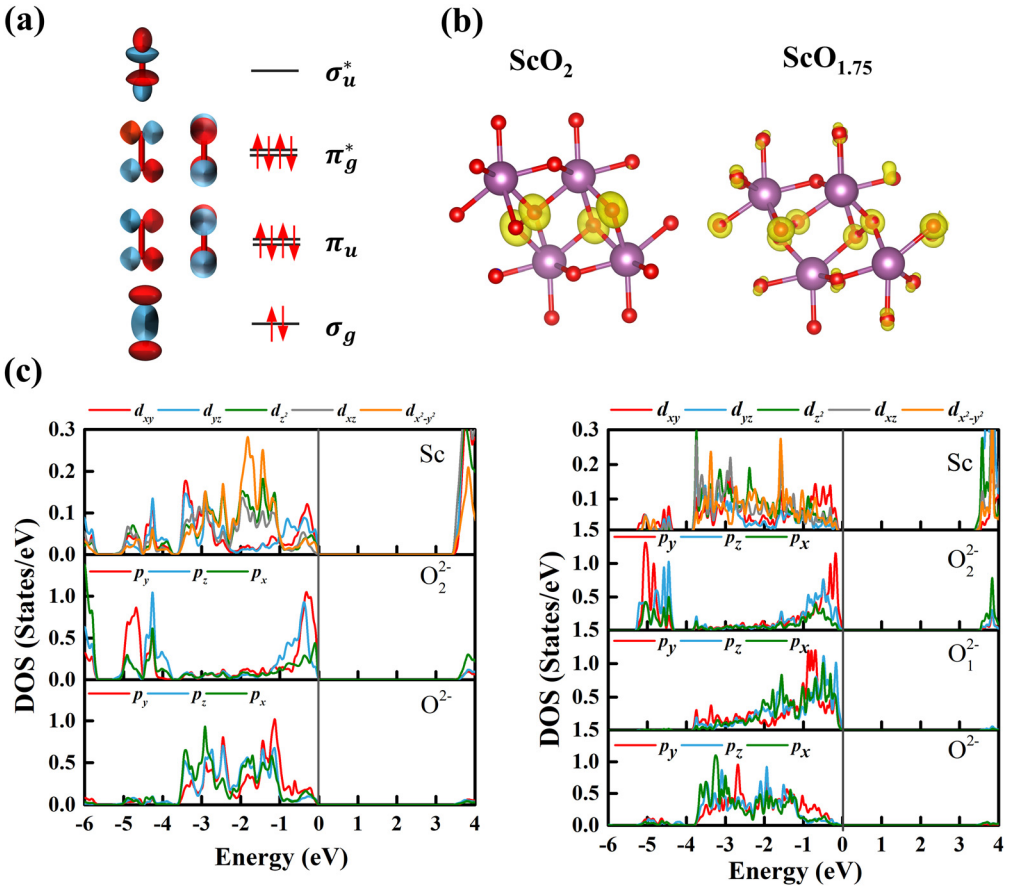

Fig. 4 (a) Molecular orbital diagram of the peroxide anion O_2^{2-}. (b) and (c) The charge densities in the energy range −0.5 to 0 eV and partial density of states (pDOS) for the atoms in ScO_2 and $ScO_{1.75}$. The zero position is the VBM. The O_1^{2-} represents the O_2^{2-} losing an oxygen atom.

where E_f denotes the formation enthalpy of each composition. The convex hulls plot clearly demonstrates the $TiO_{2.5}$ with a seven coordination configuration is the stable phase, and the phase separation fails to appear. Fig. 3(d) gives the most stable defect structure of three ordering phases: the $TiO_{2.67}$, $TiO_{2.5}$ and $TiO_{2.33}$. In the case of $TiO_{2.5}$, the O_b^{2-} shows periodic displacement in every unit cell along the x direction for the $TiO_{2.5}$, resulting in a complete seven coordinate in local structure around the Ti atoms. These ordering ground states exhibit a relatively uniform distribution of O_2^{2-} and O_b^{2-}, and satisfy the initially defined $N_c \geq 6$ and $N_w \leq 3$, which indicates the rationality of our biased screening.

3.2 Electronic properties of transition metal peroxides

One crucial difference between O_2^{2-} and O^{2-} is the presence of highly localized electrons formed by the covalent bonds of the O_2^{2-}. Fig. 4(a) shows the molecular orbitals and energy level occupancy of O_2^{2-}. The highest filled orbitals correspond to the fully occupied antibonding π_g^* orbitals in agreement with the –COHP of Fig. 2(f). In order to better understand the changes in the electronic properties induced by V_O at O_2^{2-}, we also obtain the stable phase with defects using the same calculation method as TiO_3. The average defect formation energies ΔE_{V_O} vary with vacancy concentration as shown in Fig. S3(b) (ESI†). However, with increasing oxygen vacancy concentration, the structural distortion appears greater, and the N_w is higher. Therefore, we choose pDOS of ScO_2 without the defect and $ScO_{1.75}$ with ordered V_O to compare the electronic properties, as shown in Fig. 4(c). The pDOS in the energy range −0.5 to 0 eV is mainly attributed to highly localized electrons induced by O_2^{2-} in ScO_2. The orbital hybridization between Sc^{3+} and O^{2-} is clearly observed and concentrated in the energy range −4 to −1 eV for the ScO_2 without defect.

When the ordered oxygen vacancies are introduced, the orbital hybridization between Sc^{3+} and O^{2-} weakens. Despite the O_1^{2-} failing to form antibonding π_g^* orbitals, it still has a significant contribution to the VBM rather than introducing new impurity bands within the band gap. The partial charge densities of ScO_2 without and with the defect are fully demonstrated as the VBM is mainly are contributed by O_1^{2-} and O_2^{2-}, as shown in Fig. 4(b).

Fig. 5 shows the pDOS and charge densities of TiO_3, $TiO_{2.5}$ and TiO_2. From Fig. 5(a) we can see that the pDOS near the VBM is mainly contributed by the p_z of O_2^{2-} for TiO_3, while the pDOS near the CBM is formed by the d_{z^2} of Ti^{4+}. According to the partial charge densities, we find that the charge distribution of the energy range −0.5 to 0 eV is concentrated on the O_2^{2-}. Interestingly, the p_z orbital near the VBM is due to the presence of delocalized electrons, which is significantly different from the bulk

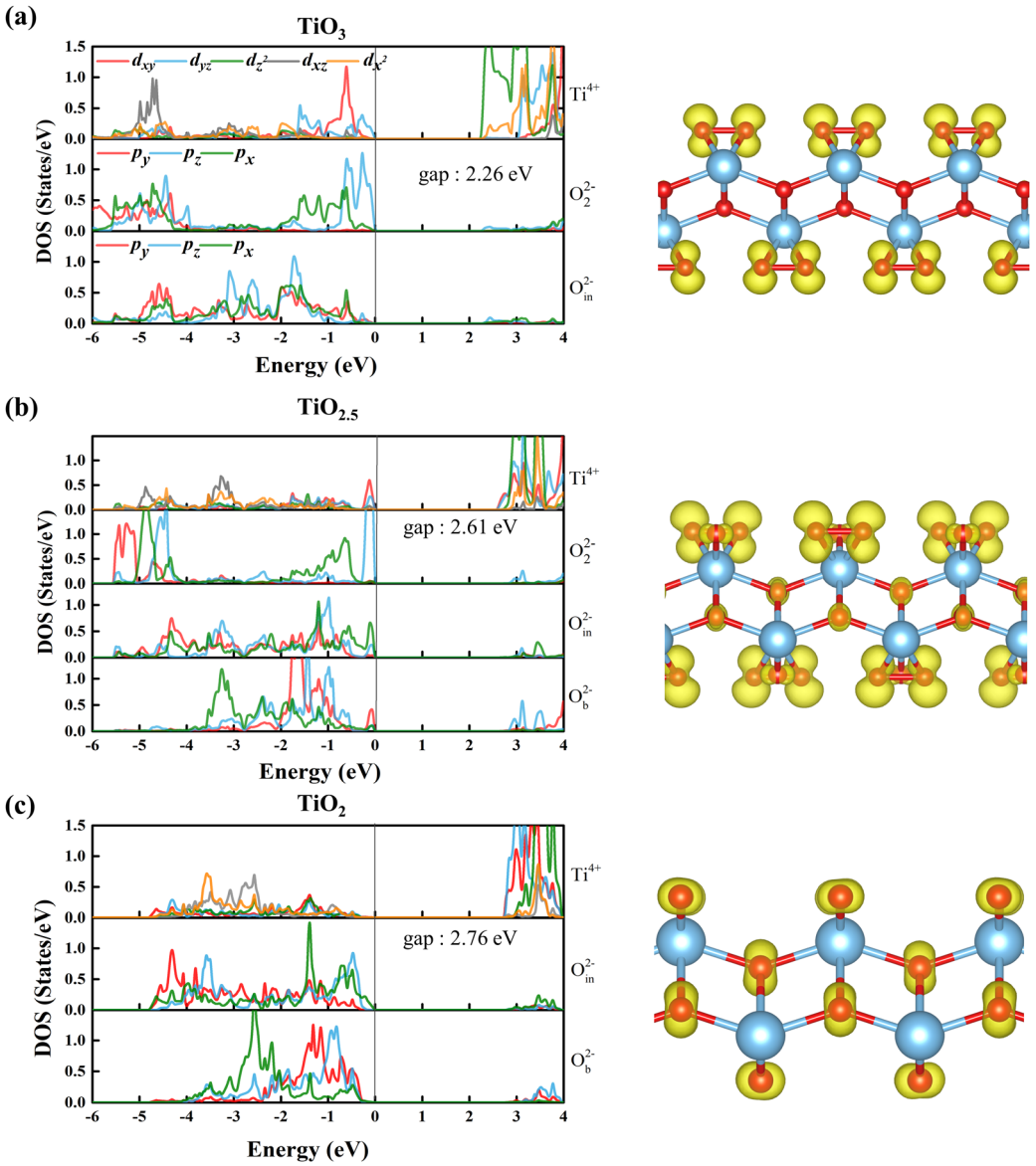

Fig. 5 (a)–(c) The pDOS and partial charge densities in the energy range −0.5 to 0 eV for the TiO_3, $TiO_{2.5}$ and TiO_2. The zero position is the VBM. The O_{in}^{2-} represents the oxygen anion in layer B.

ScO_2. The orbital hybridization between Ti^{4+} and O_2^{2-} near −0.6 eV is clearly observed. With the introduction of V_O to the surface, the orbital hybridization moves to the VBM, resulting in a narrower bandwidth, as shown in Fig. 5(b). The orbital hybridization between Ti^{4+} and O_2^{2-} near the VBM is enhanced. For the $TiO_{2.5}$, three different types of O atoms (O_2^{2-}, O_{in}^{2-}, O_b^{2-}) contribute differently to the VBM. The p_z orbitals of O_2^{2-} contribute the most, followed by the p_x of O_{in}^{2-} and the p_y of O_b^{2-}. With the introduction of the oxygen vacancy, the charges of O_2^{2-} near the VBM begin to flow to the O_{in}^{2-} and O_b^{2-}, until with the complete loss of O_2^{2-}, the VBM is mainly contributed by O_{in}^{2-} and O_b^{2-}, as shown in Fig. 5(c). Moreover, the introduction of oxygen vacancies increases the band gap. When all peroxides O_2^{2-} are lost, the band gap increases to 2.76 eV. The absence of antibonding orbital π* induced by O_2^{2-} may be one of the main reasons for the increase of band gap.

As the number of vacancies increases, the pDOS peaks of O_2^{2-} and Ti^{4+} near the VBM are much sharper and narrower than the TiO_3 without defects. This is attributed to the charges combination and the strengthening hybridization between the Ti–O. The stability of $TiO_{2.5}$ relies on the enhancement of orbital hybridization near the VBM. When the peroxide anion O_2^{2-} is completely lost, the hybridization near the VBM almost disappears. The stability of TiO_3 introducing the oxygen vacancy is the result of competition among the O_2^{2-}, O_b^{2-} and O_{in}^{2-}.

4 Conclusions

In summary, combining first-principles calculations and high-throughput methods, we have efficiently screened novel

semiconductor peroxides, such as ScO_2 and TiO_3. The clusters of Sc around seven oxygen atoms are linked by peroxide anion O_2^{2-} to form bulk ScO_2, while the layered TiO_3 has a square antiprism with metal octa-coordination. Their VBM is primarily contributed by the antibonding orbital π_g^* formed by O_2^{2-}. The V_O at O_2^{2-} is the most stable intrinsic defect, and the introduction of high concentration V_O leads to the formation of an ordered phase, such as $ScO_{1.75}$, $TiO_{2.67}$, $TiO_{2.5}$ and $TiO_{2.33}$. In both $ScO_{1.75}$ and $TiO_{2.5}$, the presence of V_O at O_2^{2-} induces charge transfer between transition metal and O atoms compared with the perfect cell. The O_1^{2-} of $ScO_{1.75}$ and O_b^{2-} of $TiO_{2.5}$ still contribute to the VBM. The continuous increase in the electronic band gaps from TiO_3 to TiO_2 can be attributed to the diminishment of antibonding orbital π_g^*. Furthermore, the presence of V_O at O_2^{2-} can strengthen the orbital hybridization of Ti–O to improve the structural stability for $TiO_{2.5}$. The discovery of transition metal peroxides not only expands the range of peroxide materials but also highlights the remarkable effectiveness of our high-throughput approach.

Conflicts of interest

There are no conflicts to declare.

Acknowledgements

This work was supported by the Guangdong Basic and Applied Basic Research Foundation (Grant No. 2021A1515010328) and the Key-Area Research and Development Program of Guangdong Province (Grant No. 2020B010183001).

References

1 M. Katayama, *Thin Solid Films*, 1999, **341**, 140–147.
2 E. Fortunato, D. Ginley, H. Hosono and D. C. Paine, *MRS Bull.*, 2007, **32**, 242–247.
3 O. Bierwagen, *Semicond. Sci. Technol.*, 2015, **30**, 024001.
4 J. Shi, J. Z. Nad Lu Yang, M. Qu, D.-C. Qi and K. H. L. Zhang, *Adv. Mater.*, 2021, **33**, 2006230.
5 K. I. Hadjiivanov and D. G. Klissurski, *Chem. Soc. Rev.*, 1996, **25**, 61–69.
6 L. Zhang, Z. Chen, J. Su and J. Li, *Renewable Sustainable Energy Rev.*, 2019, **107**, 554–567.
7 G. L. W. Hart and A. Zunger, *Phys. Rev. Lett.*, 2001, **87**, 275508.
8 G. L. W. Hart, V. Blum, M. J. Walorski and A. Zunger, *Nat. Mater.*, 2005, **4**, 391–394.
9 C.-C. He, J.-H. Liao, S.-B. Qiu, Y.-J. Zhao and X.-B. Yang, *Comput. Mater. Sci.*, 2021, **193**, 110386.
10 O. I. Malyi, M. T. Yeung, K. R. Poeppelmeier, C. Persson and A. Zunger, *Matter*, 2019, **1**, 280–294.
11 X. He, D. J. Singh, P. Boon-on, M.-W. Lee and L. Zhang, *J. Am. Chem. Soc.*, 2018, **140**, 18058–18065.
12 K. Choudhary, Q. Zhang, A. C. Reid, S. Chowdhury, N. Van Nguyen, Z. Trautt, M. W. Newrock, F. Y. Congo and F. Tavazza, *Sci. Data*, 2018, **5**, 180082.
13 A. Jain, Y. Shin and K. A. Persson, *Nat. Rev. Mater.*, 2016, **1**, 15004.
14 D. Yang, J. Lv, X. Zhao, Q. Xu, Y. Fu, Y. Zhan, A. Zunger and L. Zhang, *Chem. Mater.*, 2017, **29**, 524–538.
15 X. Shi, C. He, C. J. Pickard, C. Tang and J. Zhong, *Phys. Rev. B*, 2018, **97**, 014104.
16 A. O. Lyakhov, A. R. Oganov, H. T. Stokes and Q. Zhu, *Comput. Phys. Commun.*, 2013, **184**, 1172–1182.
17 Y. Wang, J. Lv, L. Zhu and Y. Ma, *Comput. Phys. Commun.*, 2012, **183**, 2063–2070.
18 X. Zhong, L. Yang, X. Qu, Y. Wang, J. Yang and Y. Ma, *Inorg. Chem.*, 2018, **57**, 3254–3260.
19 K. Li, J. Wang and A. R. Oganov, *J. Phys. Chem. Lett.*, 2021, **12**, 5486–5493.
20 Q. Yang, J. Lin, F. Li, J. Zhang, E. Zurek and G. Yang, *Phys. Rev. Mater.*, 2021, **5**, 044802.
21 X. Du, J. Zhang, H. Yu, J. Lin, S. Zhang and G. Yang, *Phys. Chem. Chem. Phys.*, 2020, **22**, 11460–11466.
22 Y. Wang, M. Xu, L. Yang, B. Yan, Q. Qin, X. Shao, Y. Zhang, D. Huang, X. Lin, J. Lv, D. Zhang, H. Gou, H.-K. Mao, C. Chen and Y. Ma, *Nat. Commun.*, 2020, **11**, 4702.
23 K. Gao, W. Cui, Q. Wang, J. Hao, J. Shi, S. Botti, M. A. L. Marques and Y. Li, *Phys. Rev. Mater.*, 2022, **6**, 064801.
24 A. Jain, S. P. Ong, G. Hautier, W. Chen, W. D. Richards, S. Dacek, S. Cholia, D. Gunter, D. Skinner, G. Ceder and K. A. Persson, *APL Mater.*, 2013, **1**, 011002.
25 S. Curtarolo, W. Setyawan, S. Wang, J. Xue, K. Yang, R. H. Taylor, L. J. Nelson, G. L. Hart, S. Sanvito, M. Buongiorno-Nardelli, N. Mingo and O. Levy, *Comput. Mater. Sci.*, 2012, **58**, 227–235.
26 S. Kirklin, J. E. Saal, B. Meredig, A. Thompson, J. W. Doak, M. Aykol, S. Ruhl and C. Wolverton, *npj Comput. Mater.*, 2015, **1**, 15010.
27 M. Derzsi, P. Piekarz and W. Grochala, *Phys. Rev. Lett.*, 2014, **113**, 025505.
28 S. Kirkpatrick, C. D. Gelatt and M. P. Vecchi, *Science*, 1983, **220**, 671–680.
29 D. J. Wales and J. P. K. Doye, *J. Phys. Chem. A*, 1997, **101**, 5111–5116.
30 S. Goedecker, *J. Chem. Phys.*, 2004, **120**, 9911–9917.
31 A. Laio and M. Parrinello, *Proc. Natl. Acad. Sci. U. S. A.*, 2002, **99**, 12562–12566.
32 E. Zurek, *Discovering New Materials via A Priori Crystal Structure Prediction*, 2016, pp. 274–326.
33 E. Zurek and W. Grochala, *Phys. Chem. Chem. Phys.*, 2015, **17**, 2917–2934.
34 S. Curtarolo, G. L. W. Hart, M. B. Nardelli, N. Mingo, S. Sanvito and O. Levy, *Nat. Mater.*, 2013, **12**, 191–201.
35 P. Xu, X. Ji, M. Li and W. Lu, *npj Comput. Mater.*, 2023, **9**, 42.
36 Z. Rao, P.-Y. Tung, R. Xie, Y. Wei, H. Zhang, A. Ferrari, T. Klaver, F. Körmann, P. T. Sukumar, A. K. da Silva, Y. Chen, Z. Li, D. Ponge, J. Neugebauer, O. Gutfleisch, S. Bauer and D. Raabe, *Science*, 2022, **378**, 78–85.
37 C.-C. He, J.-H. Liao, S.-B. Qiu, Y.-J. Zhao and X.-B. Yang, *Comput. Mater. Sci.*, 2021, **193**, 110386.
38 G. Kresse and J. Furthmüller, *Phys. Rev. B: Condens. Matter*, 1996, **54**, 11169–11186.

39 G. Kresse and D. Joubert, *Phys. Rev. B: Condens. Matter*, 1999, **59**, 1758–1775.
40 P. E. Blöchl, *Phys. Rev. B: Condens. Matter*, 1994, **50**, 17953–17979.
41 J. P. Perdew, K. Burke and M. Ernzerhof, *Phys. Rev. Lett.*, 1996, **77**, 3865–3868.
42 P. Giannozzi, S. de Gironcoli, P. Pavone and S. Baroni, *Phys. Rev. B: Condens. Matter*, 1991, **43**, 7231–7242.
43 S. Baroni, P. Giannozzi and A. Testa, *Phys. Rev. Lett.*, 1987, **58**, 1861–1864.
44 G. J. Martyna, M. L. Klein and M. Tuckerman, *J. Chem. Phys.*, 1992, **97**, 2635–2643.
45 S. B. Zhang, S.-H. Wei and A. Zunger, *Phys. Rev. Lett.*, 1997, **78**, 4059–4062.
46 S. P. Ong, Y. Mo and G. Ceder, *Phys. Rev. B: Condens. Matter Mater. Phys.*, 2012, **85**, 081105.
47 C.-H. Wang, D.-Y. Gui, Q. Xia, M. Avdeev, C. D. Ling and B. J. Kennedy, *Inorg. Chem.*, 2020, **59**, 14439–14446.
48 Y.-J. Cen, C.-C. He, S.-B. Qiu, Y.-J. Zhao and X.-B. Yang, *Phys. Rev. Mater.*, 2022, **6**, L050801.
49 Y. Jing, Y. Ma, Y. Li and T. Heine, *Nano Lett.*, 2017, **17**, 1833–1838.
50 N. Miao, B. Xu, N. C. Bristowe, J. Zhou and Z. Sun, *J. Am. Chem. Soc.*, 2017, **139**, 11125–11131.
51 S. Zhao, Z. Li and J. Yang, *J. Am. Chem. Soc.*, 2014, **136**, 13313–13318.
52 J. K. Burdett, R. Hoffmann and R. C. Fay, *Inorg. Chem.*, 1978, **17**, 2553–2568.

